JOURNAL OF SOLID STATE CHEMISTRY 112, 139–147 (1994)

Structural Characteristics of the 40K Superconductor $Bi_2Sr_5Cu_3(CO_3)_2O_{10}$: A HREM Study

M. Hervieu, D. Pelloquin, C. Michel, G. Van Tendeloo,[1] and B. Raveau

Laboratoire CRISMAT, ISMRA, Université de Caen, CNRS URA, 1318 Boulevard du Maréchal Juin, 14050 Caen Cedex, France

Received June 8, 1993; in revised form November 3, 1993; accepted November 5, 1993

The structural characteristics of the 40K superconductor $Bi_2Sr_5Cu_3(CO_3)_2O_{10}$ have been studied by HREM. The [110] direction allows imaging of layer stacking; the interpretation of the contrast was confirmed by image calculations. The oxycarbonate $Bi_2Sr_5Cu_3(CO_3)_2O_{10}$ exhibits a modulated structure, the angle between the c* axis and the modulation vector k being close to 29°. Intergrowth defects have been characterized as $n' = 1$ and $n' = 3$ members of the family $[Bi_2Sr_2CO_6]_n[Sr_2CuCO_3O_2]_{n'}$. Two types of oriented domains were observed: the classical 90° orientation variants and an original type which results from a superdislocation mechanism.

INTRODUCTION

The introduction of a carbonate layer in bismuth and layered cuprates has recently been evidenced by synthesis of the oxycarbonates $Tl_{0.5}A_{0.5}Sr_4Cu_2CO_3O_7$ with A = Bi, Pb (1–3) (T_c = 70 K), $Bi_2Sr_4Cu_2CO_3O_8$ (4, 5) (T_c = 30 K), and $Bi_2Sr_{6-x}Cu_3(CO_3)_2O_{10}$ (6) (T_c = 40 K). The structure of these new materials can be described as an intergrowth, along the c axis, of two kinds of layers related to the perovskite and rock salt structures. The thallium oxycarbonate structure $Tl_{0.5}A_{0.5}Sr_4Cu_2CO_3O_7$ is built up as the intergrowth of a "1201" unit, $[Tl_{0.5}A_{0.5}Sr_2CuO_5]_\infty^{1201}$, and a perovskite-related unit, $[Sr_2CuCO_3O_2]_\infty$ (7–8), according to the general formula $[Tl_{0.5}A_{0.5}Sr_2CuO_5]_n[Sr_2CuCO_3O_2]_{n'}$. Substitution of barium for strontium leads to the formation of a new structure that results from a shear mechanism (9). The bismuth oxycarbonates consist of 2201 $[Bi_2Sr_2CuO_6]_\infty^{1201}$ and $[Sr_2CuCO_3O_2]$ layers, the general formula of this new compounds being $[Bi_2Sr_2CuO_6]_n[SrCuCO_3O_2]_{n'}$. The ($n$ = 1, n' = 1) and (n = 1, n' = 2) members, $Bi_2Sr_4Cu_2CO_3O_8$ and $Bi_2Sr_{6-x}Cu_3(CO_3)_2O_{10}$, respectively, were isolated as single phases (4–6). The critical temperatures of these oxycarbonates are found to increase with the n' value: T_c = 22 K for n' = 0, T_c = 30 K for n' = 1, and T_c = 40 K for n' = 2. An electron microscopy study of the n' = 1 member showed that the different layers are, in general, highly ordered along the c axis but some crystals do exhibit intergrowth defects; the structure is furthermore modulated (5). Both phenomena are not surprising, taking into account the nature of these materials: intergrowth structures and bismuth-based phases. The present paper deals with the electron microscopy characterization of the (n = 1, n' = 2) member $Bi_2Sr_{6-x}Cu_3(CO_3)_2O_{10}$ for x = 1.

[1] On leave from the University of Antwerp (RUCA), Groenenborgerlaan 171, B-2020-Antwerp, Belgium.

2. EXPERIMENTAL

As previously reported (6), the bismuth oxycarbonates $Bi_2Sr_{6-x}Cu_3(CO_3)_2O_{10}$ were synthesized as a single phase for x ranging from 0 to 1. The $Bi_2Sr_5Cu_3(CO_3)_2O_{10}$ samples were prepared from Bi_2O_3, S_2CO_3, Sr_2CuO_3, and CuO in stoechiometric ratios and heated for short times at 880°C. The EDX analyses, performed with a KEVEX analyzer, show a ratio Bi:Sr:Cu of 2:5:3 for the x = 1 sample. The 002B electron microscope, operating at 200 kV and equiped with an objective lens with a spherical aberration ped with an objective lens with a spherical aberration constant of 0.4 mm (point resolution of 1.8 Å). Powders were ground in an agate mortar and glued on a copper grid for the high-resolution electron microscopy (HREM) study.

The powder XRD patterns have been indexed based on an orthorombic subcell as shown by E.D. (6) with a = 5.469(2) Å, b = 5.483(2) Å, and c = 54.26(1) Å.

3. RESULTS AND DISCUSSION

3.1. *Electron Diffraction*

Electron diffraction patterns along different reciprocal sections (Fig. 1) allow reciprocal space construction and deduction of the local symmetry. Without taking into account the incommensurate modulation, the structure can be described as inner-centered orthorhombic (6); the lat-

0022-4596/94 $6.00

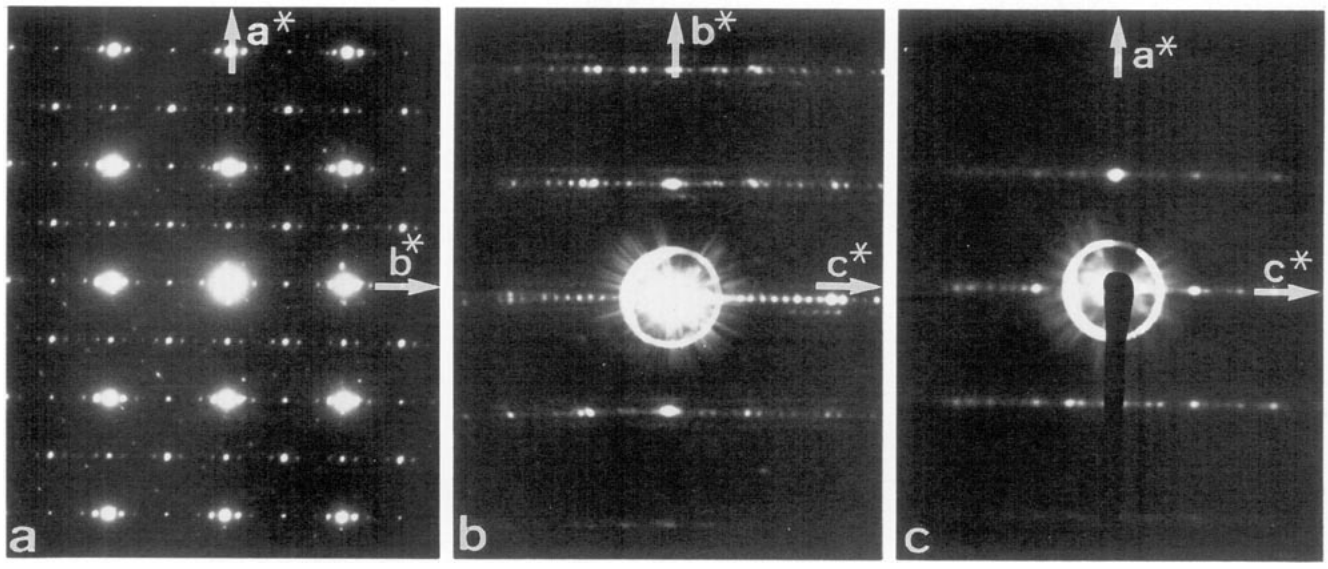

FIG. 1. Electron diffraction patterns of $Bi_2Sr_5Cu_3(CO_3)_2O_{10}$: (a) [001], (b) [100], and (c) [010].

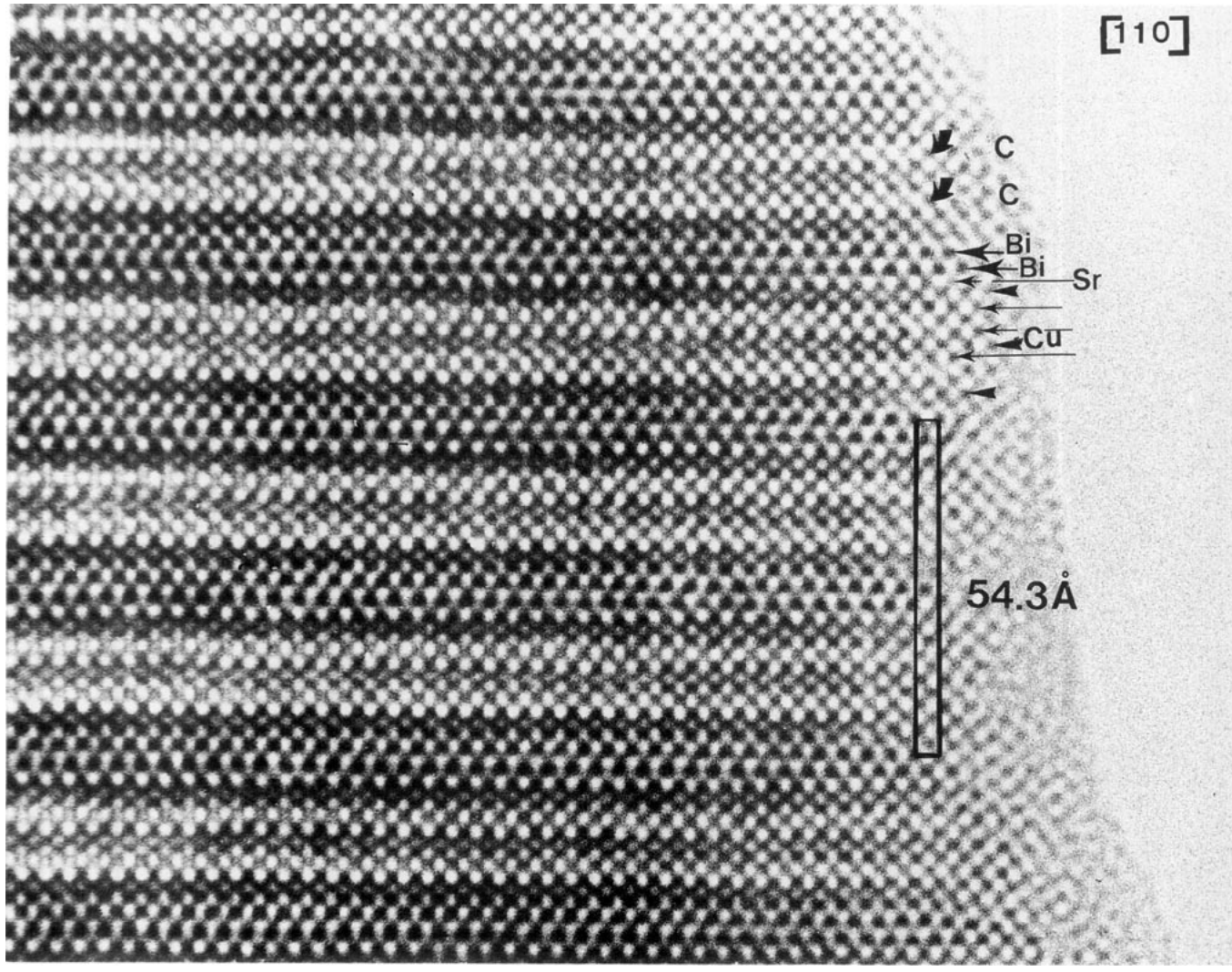

FIG. 2. [110] HREM image of $Bi_2Sr_5Cu_3(CO_3)_2O_{10}$ showing the layer stacking along the **c** axis.

tice parameters are in agreement with the X-ray results mentioned above. The modulation is obvious in the [001] and in the [100] sections in Figs. 1a and 1b. In the [100] section the satellite intensity is weak and only the first-order satellites are detectable, indicating a sinusoidal or poorly defined modulation. In fact, as we shall see from the HREM images, the crystal parts producing such patterns are always very thin, because of the highly anisotropic character of these bismuth oxycarbonates. The wave vector k (Fig. 1b) makes an angle with the **b*** axis of 61°, lowering the actual symmetry to monoclinic. The length of the wave vector is approximately 0.04 $Å^{-1}$.

3.2. *High-Resolution Microscopy*

HREM images have been obtained along several zone axes: [100], [010], [110], and [001]. All these sections provide particular information about the stacking of the layers or about the modulation.

The [110] orientation is best suited to visualize the layer stacking; Fig. 2 shows the stacking of the ideal structure for a defocus value close to the Scherzer defocus value. The darker dots are correlated with the bismuth ion columns (short arrows in Fig. 2), the three rows (per half unit cell) of gray dots with the copper ions (arrowheads in Fig. 2), and the lightest dots with the carbonate groups (curved arrows in Fig. 2); the double BiO layers are separated by six strontium layers, which are interleaved between copper and carbonate or bismuth layers (see the long arrows). This observation confirms the layer sequence [BiO–SrO–CuO_2–SrO–CO–SrO–CuO_2–SrO–CO–SrO–CuO_2–SrO–BiO] (Fig. 3) of the (n = 1, n' = 2) member of the family $Bi_2Sr_{6-x}Cu_3(CO_3)_2O_{10}$. Image calculations, based on the above structure and taking into account realistic interatomic distances usually observed in such bismuth- and carbonate-based materials, are reproduced in Fig. 4. Images were calculated for different thicknesses of 3.1, 6.2, and 9.3 nm. The latter has not been reproduced because of its similarity with that of 6.2 nm. In Fig. 4a, for a thickness of 3.1 nm, the unit cell has been outlined and the different layers can be easily be identified. For a focus value of −20 nm the different cations are imaged as black dots; this image compares with the experimental image in Fig. 2. The same unit cell has been outlined in both figures. For larger thicknesses (6.2 nm) the carbonate layers show up more clearly, as brighter or darker lines, depending on the focus value. This is also consistent with the observations of Fig. 2, where the carbonate layers in the thicker parts of the sample appear as intense bright lines.

Along the [010] direction the image recorded for a defocus value close to −50 nm exhibits a contrast characterized by a group of four rows of bright dots and two groups of two brighter rows (Fig. 5a); these brighter dots correlate to the positions of strontium and bismuth ions. The carbonate rows are hardly evidenced along this direction for any defocus value. For a defocus value close to the Scherzer value, the contrast is mainly characterized by two rows of black dots correlated to the double bismuth layers and two rows of bright dots correlated to the carbonate rows (see the curved arrows in Fig. 5b). This interpretation is confirmed by the calculated images (superposed on Fig. 5). One should note that the resolution of atomic layers is not as well defined in the experimental images as it is in the calculated images, owing to the fact that for the latter the incommensurate lattice modulation (to be discussed further) has not been taken into consideration.

The exact nature of the modulation present in the material and visualized in the diffraction patterns in Figs. 1a and 1b can be better deduced from the HREM image along [100] (Fig. 6). With the lower magnification the symmetry of the modulation is better observed, while with the higher magnification in Fig. 6b the individual lattice distortions are revealed. This image, which is recorded at a defocus value close to the Scherzer defocus value, shows the bismuth layers as rows of black dots (arrowed in Fig. 6b) and the carbonate layers as bright rows (indicated by curved arrows). Two adjacent layers modulate in antiphase, similar to the modulation in the pure bismuth cuprates and in the n' = 1 member. The difference however between the n' = 1 and the n' = 2

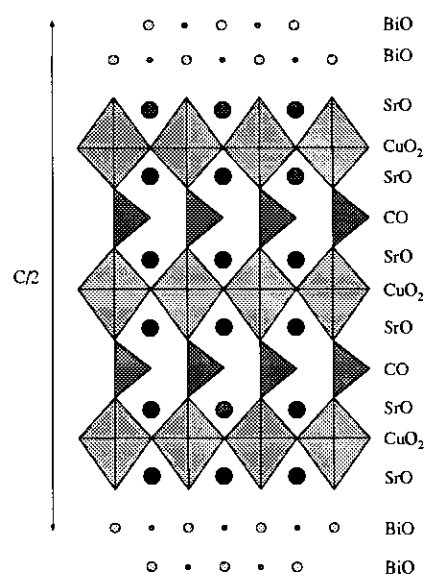

FIG. 3. Idealized model proposed on the basis of the HREM image. Only half of the unit cell is shown.

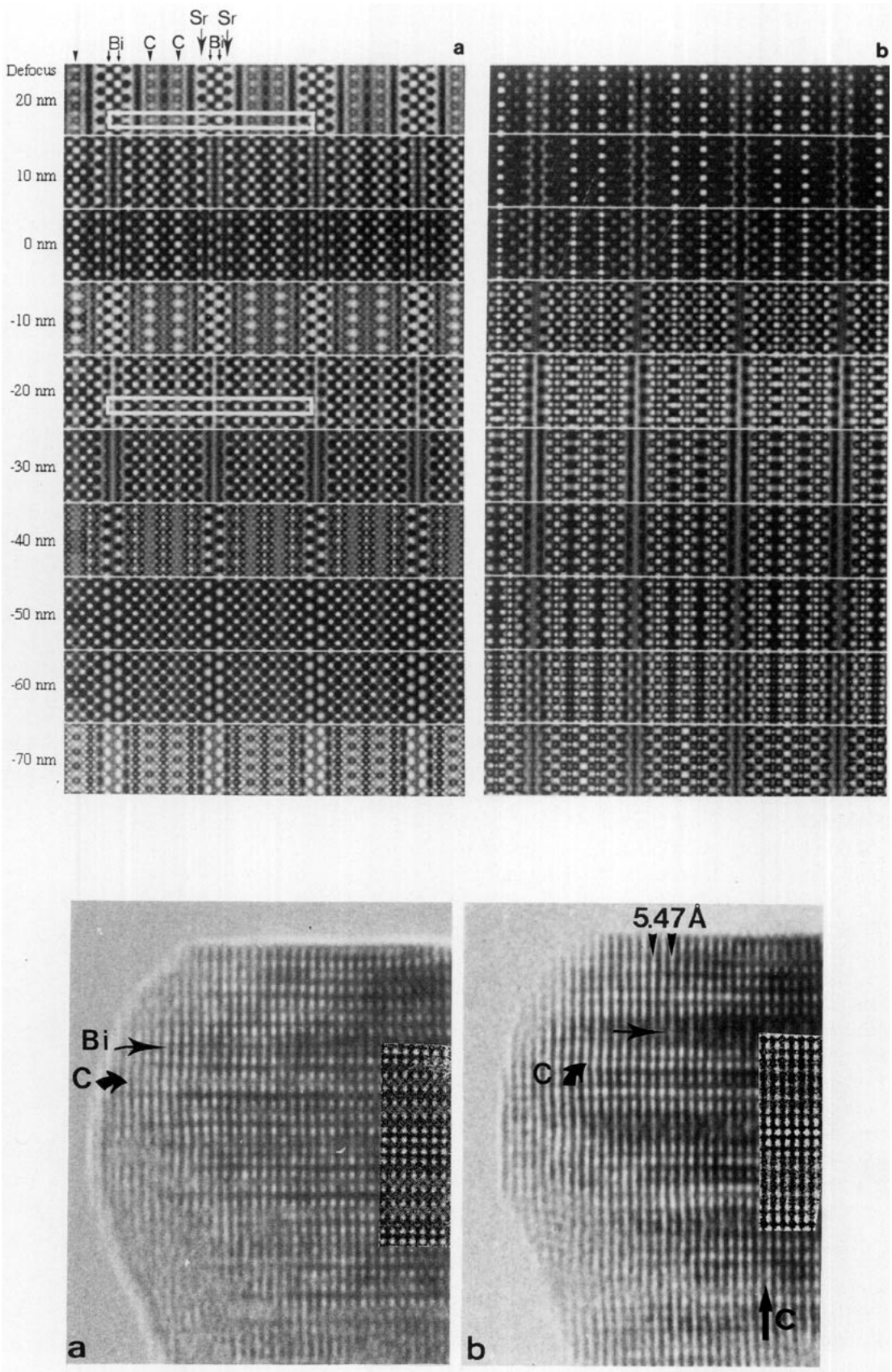

FIG. 5. [010] HREM images for focus values of (a) −500 Å and (b) −200 Å. The calculated images are shown as insets.

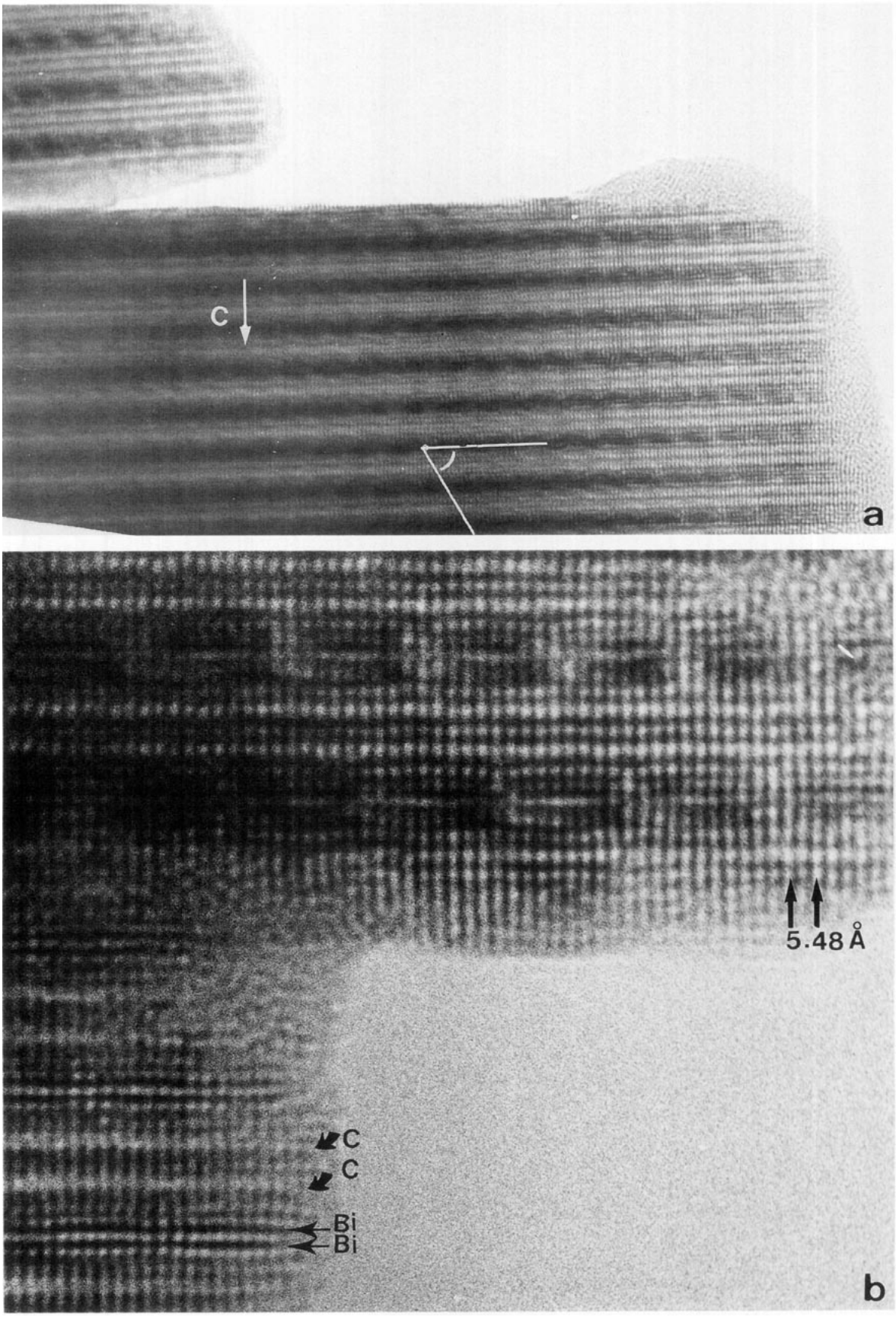

FIG. 6. [100] HREM image showing the modulated structure of $Bi_2Sr_5Cu_3(CO_3)_2O_{10}$: (a) the lower magnification and (b) the higher magnification revealing the lattice distortion.

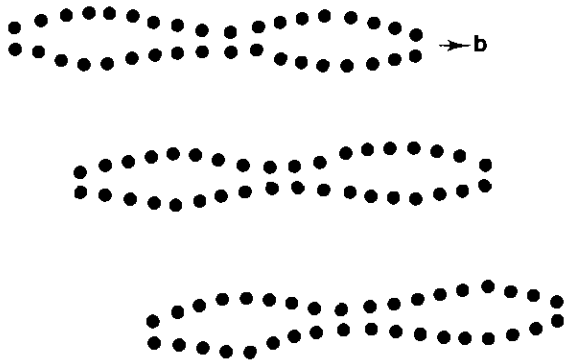

FIG. 7. Idealized representation of the double bismuth layers leading to a monoclinic modulation.

member is that for the former the modulation nodes are aligned along the **c** axis, while in the latter case the modulation is staggered along the *c* axis, lowering its symmetry to monoclinic (Fig. 7). This variation in the modulation is possibly related to the strontium deficiency of the sample ($x = 1$). It should be compared to the variation observed in the 2201 parent structure (10–12), where it was shown that the amplitude and the direction of the modulation vector vary with the barium/strontium ratio.

3.3. *Defect Structure*

In structures built from the complex intergrowth of different layers, the existence of intergrowth defects along the **c** axis is largely expected. It is surprising that actually so few stacking errors are observed. The exception is shown in Fig. 8, where one $n' = 3$ slab is surrounded by two $n' = 1$ members in a $n' = 2$ matrix. The presence of such defects can easily be detected in the [110] images by the number of carbonate rows, which under these conditions are imaged as bright rows.

Since the structure has less than tetragonal symmetry, the occurrence of 90° orientation variants, where the **a** and **b** axes are interchanged, is a common feature in this material. Similar effects have been observed in other Bi cuprates with orthorhombic or monoclinic symmetry. Such orientation variants are observed in Figs. 9 and 10 for two different directions of observation. In Fig. 9 the crystal is imaged along the [001] direction and the modulation of both orientation variants can be imaged; they are

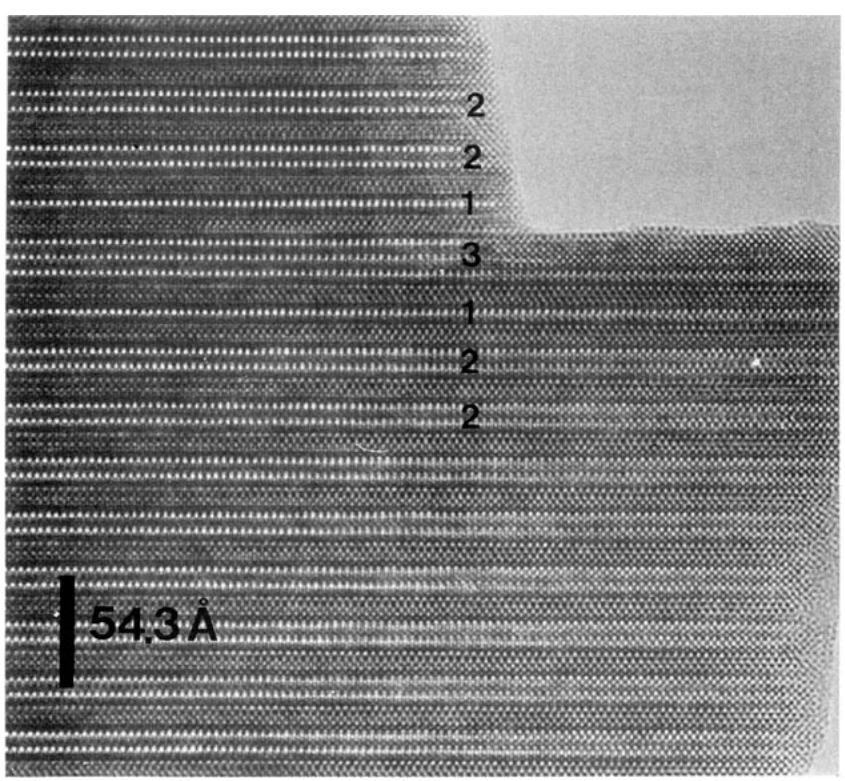

FIG. 8. [110] HREM image showing the existence of $n' = 1$ and $n' = 3$ defective slices in an $n' = 2$ matrix.

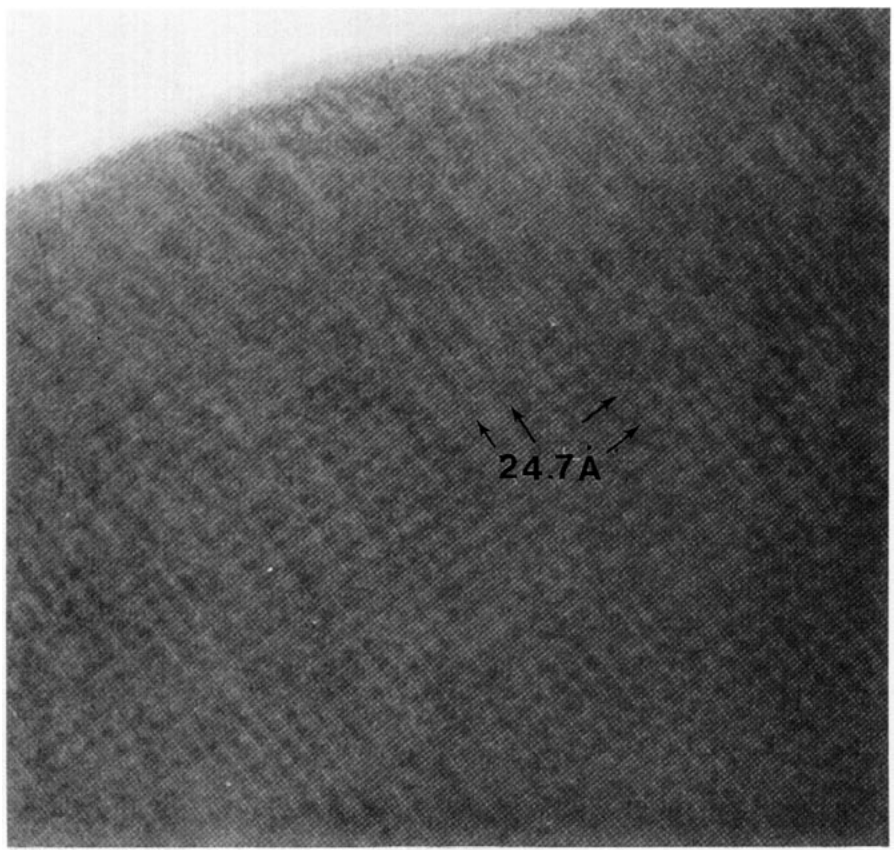

FIG. 9. [001] HREM image: the overlapping of the two 90° variants leads to a Moiré pattern.

clearly rotated over 90° and they overlap in some parts, resulting in a Moiré pattern.

In Fig. 10a the crystal is imaged parallel to the (001) plane; the top part is oriented along [100], where the modulation is clearly visible, while the middle part is oriented along [010]. This image also illustrates the mica-like morphology of the crystals, similar to that observed in the bismuth cuprates and in the $n' = 1$ member of the family. This layerlike pheonomenon is sometimes enhanced by the existence of slices of amorphous material (labeled A). Also visible in Fig. 10a are two subgrain boundaries (white arrows) inducing a rotation of about 11° along the [010] axis. This angle remains constant in several crystals. In the enlargement of Fig. 10b it is clear that this subgrain boundary involves the presence of superdislocations. In the top part, marked 1, the distance along **a**, limited by two arrows, contains 14 octahedra while this number increases to 16 (area 2) and finally to 18 (area 3) for the lower part between the corresponding arrows. This misorientation can be explained by the schematic model given in Fig. 11, which shows that the misorientation between the left and right parts of the crystal is due to the introduction of two (100) oxycarbonate slices (see the rectangle in Fig. 11) according to the sequence "Sr–Cu–Sr–"CO_3"–Sr–Cu–Sr–CO_3–Cu–Sr" along **a**.

4. CONCLUSION

High-resolution electron microscopy of the $Bi_2Sr_5Cu_3(CO_3)_2O_{10}$ oxycarbonate showed that the material can be considered as a regular stacking along the **c** axis of one 2201 unit and two $Sr_2CuCO_3O_2$ units.

The structure is further modulated ($\lambda = 24.7$ Å), the angle between the **c*** axis and the modulation vector **q** being close to 29°. The exact orientation of this modulation vector is probably related to the exact strontium content in the material. Similar phenomena have been observed previously in the 2201 parent structure.

The crystals are mostly perfect, but some intergrowth defects are observed corresponding to the presence of $n' = 1$ and $n' = 3$ members of the family $[Bi_2Sr_2CuO_6]_n$ $[Sr_2CuCO_3O_2]_{n'}$. Other defects observed correspond to the "classical" 90° orientation twins. Several misorientations have been observed; they are shown to be introduced by the presence of superdislocations.

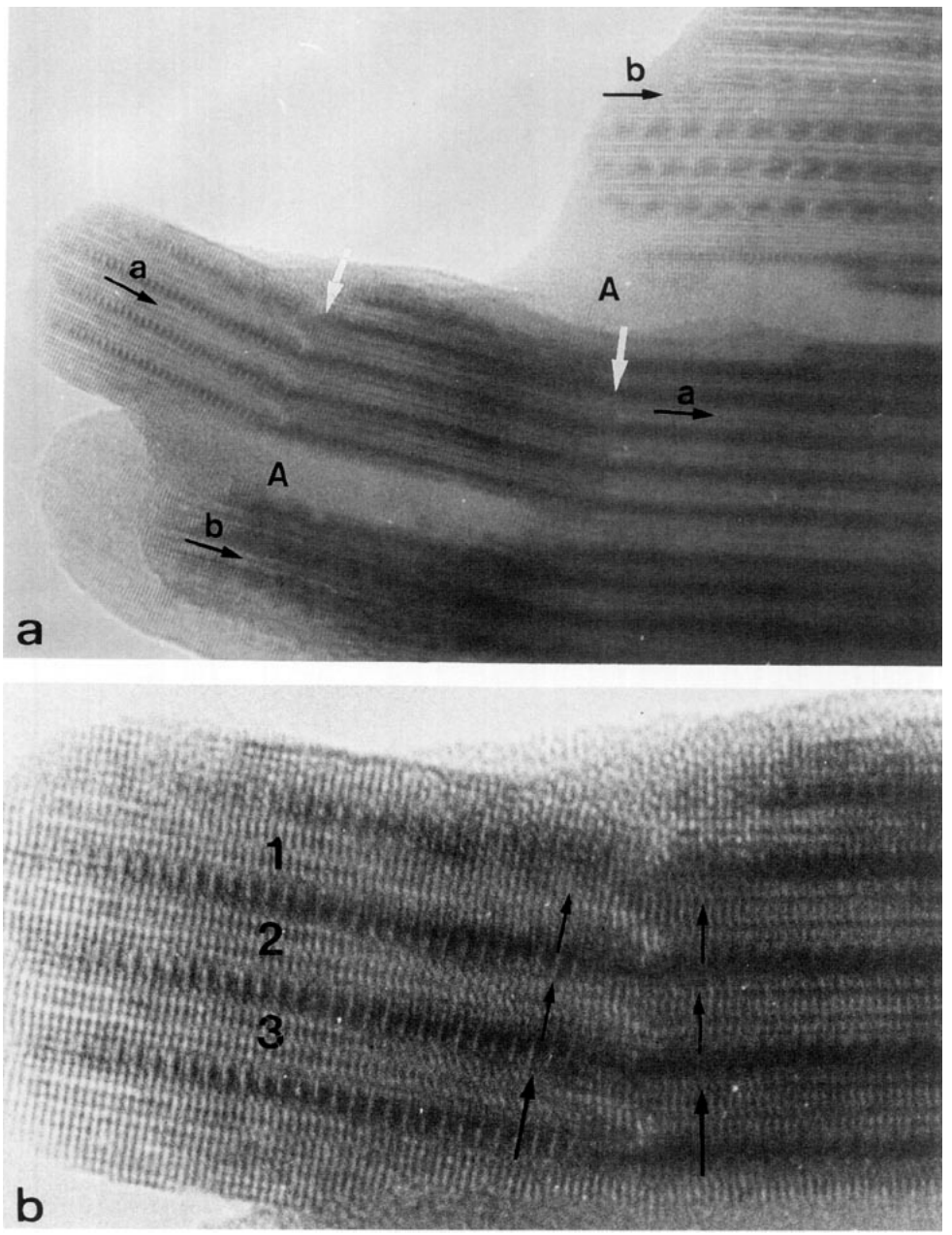

FIG. 10. Stacking of 90° oriented parts along **c**. Note the micalike morphology of the crystal and the existence of amorphous slices (labeled A). (a) Low magnification; two subgrain boundaries are indicated by white arrows. (b) Enlargement of a subgrain boundary arising from a superdislocation mechanism.

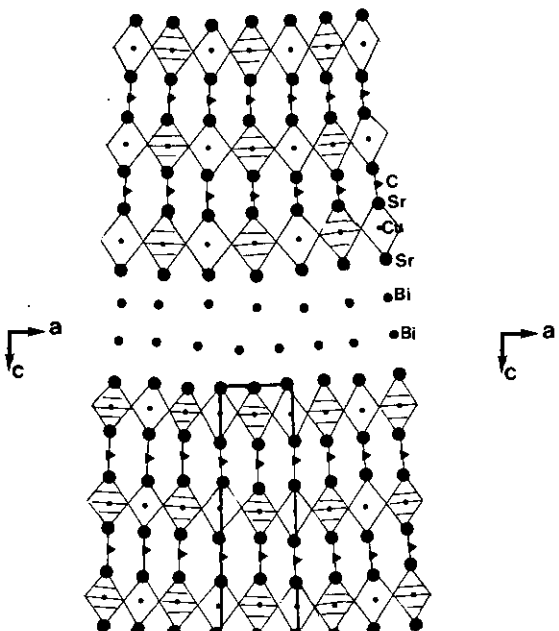

FIG. 11. Idealized model of the boundary; the misorientations between the two parts of the crystal are due to the introduction of (100) oxycarbonate slices (rectangle).

REFERENCES

1. M. Huvé, C. Michel, A. Maignan, M. Hervieu, C. Martin, and B. Raveau, *Physica C* **205,** 219 (1993).
2. A. Maignan, M. Huvé, C. Michel, M. Hervieu, C. Martin, and B. Raveau, *Physica C* **208,** 149 (1993).
3. M. Hervieu, C. Michel, M. Huvé, C. Martin, A. Maignan, and B. Raveau, *Microsc. Microanal. Microstruct.* **1** (1993).
4. D. Pelloquin, M. Caldes, A. Maignan, C. Michel, M. Hervieu, and B. Raveau, *Physica C* **208,** 12 (1993).
5. M. Hervieu, M. T. Caldes, C. Michel, D. Pelloquin, and B. Raveau, *J. Solid State Chem.* **108,** 346 (1994).
6. D. Pelloquin, A. Maignan, M. Caldes, H. Hervieu, C. Michel, and B. Baveau, *Physica C,* in press.
7. T. G. Babu, D. J. Fish, and C. Greaves, *J. Maser Chem.* **14,** 677 (1991).
8. Y. Miyazaki, H. Yamane, T. Kajitani, T. Oku, K. Hiraga, Y. Morii, K. Fuchizaki, S. Funashashi, and T. Hirai, *Physica C* **191,** 434 (1992).
9. F. Goutenoire, M. Hervieu, A. Maignan, C. Martin, and B. Raveau, *Physica C* **210** (1993).
10. Z. Hiroi, Y. Ikeda, M. Takano, and Y. Bando, *J. Mater. Res.* **6,** 435 (1991).
11. Y. Shen, D. R. Richards, D. G. Hinks and A. W. Mitchell, *J. Mater. Res.* **7,** 844 (1992).
12. B. C. Chakoumakos, J. D. Budai, B. C. Sales, and Edward Sonder, *Mater. Res. Soc. Symp. Proc.* **156,** 329 (1989).